Title: Tsunamigenic earthquake simulations using experimentally derived friction laws

S. Murphy[1,2*], G. Di Toro[3,4], F. Romano[1], A. Scala[1], S. Lorito[1], E. Spagnuolo[1], S. Aretusini[3], G. Festa[5], A. Piatanesi[1], S. Nielsen[6]

[1]Istituto Nazionale di Geofisica e Vulcanologia, Rome, Italy

[2]Ifremer, Plouzané, France

[3]University of Manchester, Manchester, United Kingdom

[4]Università degli Studi di Padova, Padua, Italy

[5]Università di Napoli Federico II, Naples, Italy

[6]Durham University, Durham United Kingdom

*shane.murphy@ifremer.fr

Keywords: subduction zone; megathrust; dynamic rupture; rock physics experiments; tsunami earthquake

Abstract

Seismological, tsunami and geodetic observations have shown that subduction zones are complex systems where the properties of earthquake rupture vary with depth as a result of different pre-stress and frictional conditions. A wealth of earthquakes of different sizes and different source features (e.g. rupture duration) can be generated in subduction zones, including tsunami earthquakes, some of which can produce extreme tsunamigenic events. Here, we offer a geological perspective principally accounting for depth-dependent frictional conditions, while adopting a simplified distribution of on-fault tectonic pre-stress.

We combine a lithology-controlled, depth-dependent experimental friction law with 2D elastodynamic rupture simulations for a Tohoku-like subduction zone cross-section. Subduction zone fault rocks are dominantly incohesive and clay-rich near the surface, transitioning to cohesive and more crystalline at depth. By randomly shifting along fault dip the location of the high shear stress regions ("asperities"), moderate to great thrust earthquakes and tsunami earthquakes are produced that are quite consistent with seismological, geodetic, and tsunami observations. As an effect of depth-dependent friction in our model, slip is confined to the high stress asperity at depth; near the surface rupture is impeded by the rock-clay transition constraining slip to the clay-rich layer. However, when the high stress asperity is located in the clay-to-crystalline rock transition, great thrust earthquakes can be generated similar to the M_w 9 Tohoku (2011) earthquake.

1. Introduction

Seismological, geodetic, and tsunami observations have shown that subduction zones are complex systems where the properties of earthquake rupture vary with depth (Lay et al., 2012). For example, earthquake duration normalized for event size has been observed to decrease with depth; this recurrent feature has been attributed to depth varying shear modulus and / or stress drop for individual earthquakes (Bilek and Lay, 1999; Bilek et al., 2016; Geist and Bilek, 2001). Depth variation in subduction ruptures is, for example, evident when comparing the different historical earthquakes that occurred off the Pacific coast of Tohoku region in Japan (Fig. 1). A number of major (M_w 7-7.9) thrust earthquakes mostly slipped within a depth range of 10 – 40 km. These events involved individual patches of concentrated slip implying the breaking of at least one prominent, high stress asperity (Shao et al., 2011; Yamanaka and Kikuchi, 2004). Conversely, the 1896 Meiji event (M 8.2 – 8.4), likely involved slip primarily at the base of the shallow accretionary wedge or beneath it. This earthquake produced a disproportionately large tsunami relative to its moment magnitude, possibly making it a potential 'tsunami earthquake' (Kanamori, 1972). The great M_w 9.0 2011 Tohoku earthquake nucleated at ~20 – 25 km depth, and produced slip at traditionally expected depths while also realising a substantial amount of slip all the way to the trench (i.e., at less than 10 km depth) (Chu et al., 2011; Ide et al., 2011; Romano et al., 2014).

Numerical models of the dynamic rupture process have successfully described either individual types of earthquakes, for example the Tohoku event (Kozdon and Dunham, 2013; Noda and Lapusta, 2013), or both thrust and tsunami earthquakes in the same model (Mitsui and Yagi, 2013). Numerical models coupled with the rate-and-state friction law have been used to reproduce full seismic cycles for subduction environments. However, this comes at the expense of either failing to account for geometry / free surface effects and inhomogeneity in the material surrounding the fault (Cubas et al., 2015; Noda and Lapusta, 2013), or by simplifying wave propagation to static stress changes on the fault plane (Shibazaki et al., 2011). Fully dynamic simulations including a free surface and variable geometry have tended to focus on specific rupture features of the Tohoku earthquake such as the slip in the trench or long period guided wave propagation in the ocean (Hirono et al., 2016; Huang et al., 2013; Kozdon and Dunham, 2014). Depth dependent changes in frictional parameters have been tested using rate-and-state models for the 2011 Tohoku (Kozdon and Dunham, 2013). However, to our knowledge, no numerical model has been able to reproduce a range of different observed earthquakes types (e.g. Fig. 1) while at the same time accounting for the fault geometry and complex structure as proposed here.

The focus of this study is to provide a simple yet geologically consistent model that reconciles the different observed earthquake types with fault properties from independent theoretical and laboratory studies. We focus our investigation on the aspect of rupture dynamics due to depth-dependent frictional conditions focusing on a specific time window of the seismic cycle including the sub-seismic frictional properties of the fault materials (Den Hartog et al., 2012). Hence, the friction law parameters were chosen based on available geological and geophysical constraints. On the other hand, investigating inter-seismic and nucleation processes is beyond the scope of this study. As a consequence, the set up for the numerical model was simplified, particularly as far as the initial stress distribution is concerned. While the initial stress is heterogeneous, being the derivative of a composite slip model (Murphy et al., 2016), it is highly localized. Moreover, since a 2D model is used, we do not address the influence of lateral variations on rupture features.

2. Numerical Model

We modelled the earthquake rupture dynamics (Festa and Vilotte, 2006) on a 2D cross-section through a Tohoku-like fault (Figs. 2a-d). Dynamic rupture is simulated using a 2D non-smooth spectral element method (Festa and Vilotte, 2005). The curved fault geometry is based on Slab 1.0 (Hayes et al., 2012) which has been slightly modified so that the subduction interface extends to the surface. The media is heterogeneous with the layers and their elastic properties (described in Fig. 2 and Table S1 in *Supplementary Material*) based on a seismic survey in the zone of the 2011 Tohoku earthquake (Miura et al., 2005).

2.1 Laboratory derived thermal weakening friction law

A thermal slip weakening empirical friction law was used in all simulations which is particularly suitable for representing dynamic weakening observed in a regime of slip velocities that rapidly accelerate to seismic slip rates. There are a number of other empirical friction laws (e.g., linear slip weakening (Ida, 1972); rate-and-state (Dieterich, 1979; Ruina, 1983)). We have chosen the thermal weakening friction law as it is based on rock physics experiments performed at slip-rates expected during large earthquakes using materials typical in subduction zones.

This law is based on laboratory observations of the evolution of friction with slip in a rotary shear machine where cohesive (serpentinites, peridotites, gabbros, basalts, marbles, granitoids, sandstones, etc.) and non-cohesive (clay-rich gouges, serpentinite gouges, basalt gouges, etc.) rocks were tested over a quite large range of slip rates (0.1 to 6.5 m/s), accelerations (0.5 to 65 m/s^2), normal stresses (5 to 95 MPa), ambient conditions (room humidity to fluid saturated) and displacements (0.3 to 50 m) expected during moderate to large earthquakes (Di Toro et al., 2011). A common feature from this extensive set of experiments is that the evolution of friction with slip can be described by an exponential decay to a first order approximation. This dependency is defined as:

$$\mu\,(\delta) = \mu_d + (\mu_s - \mu_d)e^{\frac{-\delta}{d_{th}}} \qquad \text{(Eq. 1)}$$

where μ_s and μ_d are the static and dynamic friction coefficients, respectively, and depend on material type. The co-seismic slip is δ and d_{th} the thermal weakening distance. For a suite of experiments performed at a variety of slip rates and normal stresses, d_{th} was shown to have an inverse relationship with the normal stress σ_n:

$$d_{th} = \alpha \, \|\sigma_n\|^{-\beta} \qquad \text{(Eq. 2)}$$

with α ranging between 3 - 78 depending on material type (Di Toro et al., 2011) and β = 1 (Nielsen et al., 2010). This friction law produces a similar exponential evolution of fault strength with slip to that observed by Hirono et al. (2016) whose numerically modelled thermal pressurization on the Japan Trench using expected permeability and porosity for the region.

2.2 Variation in fault material

Depth dependent frictional parameters were chosen based on expected dominant rock types in mega-thrust environments (Hacker et al., 2003a; 2003b; Kimura et al., 2012; Meneghini et al., 2010). Initially unconsolidated and, in the case of Tohoku, clay-rich sediments (Chester et al., 2013), undergo compaction, dehydration, diagenesis and metamorphism into crystalline rocks (phyllites, schists, calc-schists, marbles, quartzites, etc.) due to increasing pressure and temperature during burial (Hacker et al., 2003b; 2003a; Hyndman et al., 1997; Ikari et al., 2007; Kimura et al., 2012). Consequently, high velocity experiments on peridotite (Del Gaudio et al., 2009) were taken as a proxy for mantle rock (i.e., μ_s = 0.7, μ_d = 0.25, α = 78), however gabbro, basalts and serpentinite have similar frictional properties when sheared under seismic deformation conditions (Niemeijer et al., 2011; Proctor et al., 2014; Violay et al., 2014). For clay-like material the static and dynamic coefficients of friction were set to 0.25 and 0.1 respectively based on experiments performed under room humidity conditions and in the presence of liquid water

(Remitti et al., 2015; Sawai et al., 2014; Ujiie et al., 2013). Experimental studies from literature were used to determine the α value used for the clay-like material in the numerical model (see Fig 3 and Table S3 in Supplementary Material). Most of the latter experiments were performed at room humidity on a variety of different clay minerals and under increasing normal stresses. Ideally, data from experiments on unconsolidated wet clay materials would be used. However, experiments at high normal stress (> 20 MPa) are very challenging on these materials and not enough data exist to calculate the variation of d_{th} with normal stress. Setting $\beta = 1$ based on theoretical findings (Nielsen et al., 2010), $\alpha = 3.712$ provided the best fit for equation 2 to the experimental data (see Fig. 3) with a R-square of 0.735 and a 95% confidence bounds of 3.32 to 4.11. Below 40 km d_{th} was artificially increased to 20 m in order to act as a numerical barrier to rupture at the bottom of the fault. This depth was chosen as it corresponds to the depth at which co-seismic slip in the 2011 M_w 9.0 Tohoku earthquake rapidly decreased and the largest post-seismic slip occurred (Ozawa et al., 2011). This is also the estimated depth where creep begins (Freed, 2005).

Using an effective basal friction of 0.03, thermal modelling of the Tohoku fault (Kimura et al., 2012) places the 50°C isotherm at 10 km depth and 150°C isotherm at a depth of 20 km. Guided by these findings, we defined the frictional parameters above 2 km as clay-like, with a linear transition to rock-like frictional parameters in the 12-20 km depth range. This interval accounts for peak dehydration due to opal to quartz and smectite to illite conversion rates estimated to occur at 12 km depth (Kimura et al., 2012). This transformation is consistent with experimental findings on clays that showed only a minor increase in the coefficient of friction as a function of smectite-to-illite transformation and effective normal stress (i.e. from 0.27

to 0.4) (Saffer et al., 2012). However, there is a significant increase in the friction coefficient associated with a decrease in water content (e.g. by dehydration), or an increase in quartz content in the system (e.g. by silicization and/or precipitation of quartz veins) (Ikari et al., 2007).

2.3 Bi-material fault surface

The subduction interface is on the boundary between the oceanic lithospheric layer and various hanging-wall materials (e.g., wedge and various mantle layers that vary with depth) which can lead to ill-posedness and numerical instability in terms of modelling due to the bi-material propagation (Cochard and Madariaga, 1996). To accommodate for this, the evolution of the normal stress is regularized whereby the frictional strength depends on the evolving normal stress σ_e that, in turn, varies due to normal stress perturbations σ_n depending on either a slip-rate-based or a constant characteristic time scale (Rubin and Ampuero, 2007):

$$\frac{d\sigma_e}{dt} = \frac{\alpha_e |v| + v^*}{\delta_D}(\sigma_n - \sigma_e) \qquad \text{(Eq. 3)}$$

where v^* is a characteristic slip rate, δ_D a characteristic slip scale, $|v|$ is the local value of slip rate, and α_e can assume the values 0 or 1. For this study, $v^* = 0$, $\alpha_e = 1$, and $\delta_D = 0.3\, d_{th}$ were used as they were found to produce numerically stable and physically convergent solutions (Scala et al., 2017). The relationship between the classical slip weakening distance, d_c and the thermal weakening distance, d_{th}, is $d_c \approx 3d_{th}$ (Di Toro et al., 2011).

2. 4 Presence of fluids

In order to account for the effect of fluids we consider the dynamic Coulomb wedge theory (Wang and Hu, 2006) which proposes that fluid pressure ratio, λ, and effective basal friction, defined as $\mu_b' = \mu(1-\lambda)$ (Wang et al., 2010) where μ is the coefficient of friction, vary between the front, middle and back of the forearc prism. Based on analysis of seismic profiles and thermal models (Kimura et al., 2012), λ = 0.9 was applied to the section of the fault at the back of the prism with λ = 0.95 (depth > 14.6 km) for the middle section of the prism (depth range of 9.6 – 14.6 km). For the frontal section of the prism (< 9.6 km), λ = 0.65 was used. Assuming that μ is similar to the static friction coefficient used in our dynamic simulations (i.e., $\mu = \mu_s$) we can compare our initial conditions with other studies. The initial conditions for our numerical model exhibits μ_b' of 0.0875, 0.0125 and 0.025 to 0.07 for the front, middle and back sections of the accretionary wedge which is comparable to observations (i.e., > 0.08, < 0.03 and 0.03 for the respective sections of the prism) (Kimura et al., 2012) and $\mu_b' = 0.025$ for the whole fault (Gao and Wang, 2014). Using this depth dependent λ, the principal vertical component of stress was estimated as the difference between lithostatic normal load and hydrostatic pore pressure using the principal vertical stress $\sigma_3 = (1-\lambda) g\, \rho\, z$, where g is the gravity, ρ is the density and z is the depth. The fluid retention depth, Z_{FRD}, is the point at which fluid pressure increases at the same rate as the lithostatic gradient (Suppe, 2014). It defines the strength of the fault at depth: the deeper Z_{FRD} is, the stronger the fault becomes, and if all other parameters are similar, the larger the potential stress drop could be during rupture below Z_{FRD}. We assumed Z_{FRD} ~12 km, the point at which the transformation of the frictional parameters from clay-like to rock-like has ended. Therefore, σ_3 tracks the lithostatic gradient below z_{FRD}. The horizontal principal stress, σ_1, was set to 4.05

σ_3 (see Section A2 in *Supplementary Material* on discussion on choice for this scaling factor). The effective normal stress on the fault is calculated based on fault geometry relative to the two principal components of stress. The fault strength, that is the stress at which the fault fails, is a function of the static friction coefficient and the effective initial normal stress (black dashed line in Fig. 4a).

2.5 Initial shear stress distribution

As discussed in the introduction, many of the historical thrust earthquakes in the Tohoku region (Fig. 1), can be described with one patch of heterogeneous but concentrated significant slip suggesting that only one major high shear stress “asperity” might have failed at the yield stress in these events. While this may not be always the case, as earthquakes exhibit in general a large variability in the complexity of their slip distributions (e.g. Lorito et al., 2016), a simplified single high stress asperity model is used here, where the initial stress is spatially concentrated in different locations along the fault plane. In reality, the initial shear stress on the fault plane varies both spatially and temporally and is dependent on a number of phenomena such as loading rate, coupling, and historical earthquakes (Nalbant et al., 2013).

In order to control the location of the high stress asperity, the initial shear stress distribution was generated by taking the spatial derivative of a 1D heterogeneous slip distribution constructed using a composite source model (Murphy et al., 2016). The location of the high stress asperity is placed randomly on the fault plane for each simulation. The maximum allowable shear stress in the model is defined by the fault strength, meaning that asperities in the crystalline rock material contain higher stress compared with asperities in clay-like material. Nucleation is achieved by lowering the effective normal stress such that the fault strength is a few percent below the initial shear stress (see Fig. S2 in *Supplementary Material* for examples). The location of the nucleation is randomly chosen to be within the asperity on the fault.

3. Results

Initially, three separate simulations with asperity locations at different depths were chosen (15 km, 19 km and 36 km) as a case study (Fig. 4a). These three simulations are referred to as "shallow" (blue), "intermediate" (orange) and "deep" (purple) in reference to the relative location of the three asperities. Later this procedure is extended to 45 simulations with asperity locations randomly chosen between 10 - 40 km depth.

3.1 Breakdown Energy

The three simulations produce radically different slip distributions (Fig. 4b): the deep asperity produced a concentrated patch of slip (maximum slip of 16 m); the intermediate asperity produced the largest earthquake (maximum slip of 38 m) with surface rupture; while the shallow asperity produced the smallest earthquake (maximum slip of 9.5 m). The differences in the amount of slip and earthquake size in our model can be traced back to the depth variation of the fault strength (Fig. 4a) and its evolution with slip (Fig. 4c). This depth dependence in turn plays an important role in controlling the interplay between the release of stored elastic energy and breakdown energy, G_b^i. The breakdown energy G_b^i has been calculated by numerically integrating the evolution of shear stress over the slipping distance using the formula (Abercrombie and Rice, 2005):

$$G_b^i = \int_0^{\delta} [\tau(\delta') - \tau(\delta)]\, d\delta' \qquad \text{(Eq .4)}$$

where δ is the total slip. The G_b^i was calculated of each point on the fault where co-seismic slip occurs in the three case studies depicted in Fig 4. The amount of energy required to propagate the rupture dramatically increased below 17 km depth by at least a factor of 50 as shown in Fig. 5a.

3.2 Energy Release Rate

The stress drop, $\Delta\sigma$, systematically increased from 4 MPa to 20 MPa with increasing depth (Fig. 5b). The static stress drop has been calculated using $\Delta\sigma = \tau_o - \tau_f$ where τ_f is the shear stress at the end of rupture and τ_o is the initial shear stress (Kato, 2012). Negative stress drop may occur (as is the case in Fig. 5b) when the stress at a point on the fault is higher at the end of the simulation than at the start. This can occur beyond the arrest region of the earthquake where fault strength does not evolve to residual dynamic strength and therefore the stress in this zone is at a higher level relative to before the earthquake. Negative stress drops may also occur when the initial stress is less than the dynamic strength of the fault ($\tau_o < \mu_d\sigma_n$), in such cases rupture can continue to propagate in these unfavourable zones for a limited distance depending on the energy release rate and G_b^i (Kozdon and Dunham, 2013).

Taking the square of the static stress drop as a proxy for the energy release rate ($G^* \propto \Delta\sigma^2$, assuming rupture velocity remains constant (Nielsen et al., 2016)), this latter quantity increased by a factor of 25 with depth. This depth-dependent relative difference between G_b^i and G^* made it difficult for rupture to propagate out of the trench zone. Therefore, earthquakes that nucleate in shallower clay-rich lithology are more likely to propagate along strike rather than down-dip producing the large length-to-width ratios observed for tsunami earthquakes (e.g., 1896 Meiji (Tanioka and Satake, 1996), 1992 Nicaragua (Ihmlé, 1996), 2006 Java (Ammon et al., 2006)).

3.3 "Shallow" earthquakes

Comparing the deepest and shallowest nucleating earthquakes in Fig. 4a, both have comparable duration (Fig. 6a) and tsunami source amplitude (Fig. 6b and Section A3 in *Supplementary Material*) despite the latter being smaller in size; these findings make the shallowest event in principle compatible with a tsunami earthquake (Grezio et. al., 2017; Satake and Tanioka, 1999). Additional simulations reveal that earthquakes with centroid depth (i.e., the average depth of the slipping area of the earthquake weighted by the slip) located in the high pore pressure zone under the accretionary wedge had consistently longer normalized rupture durations (duration of earthquake has been normalized with respect to moment, see Section A4 in *Supplementary Material*) when compared with earthquakes from other zones on the fault (Fig. 7a). This is a systematic feature in our simulations and it is also consistent with seismological observations (Bilek and Lay, 1999). This depth dependent variation of rupture duration is due to a decrease in both the average stress drop and rigidity (Figs. 7b-c) at shallow depths confirming the hypothesis that rupture duration is linked with depth varying mechanical properties (Bilek and Lay, 1999). Additionally, for earthquakes where significant slip is in the high pore pressure zone the average rupture velocities were in the range of 1.2–2.2 km/s (Fig. 7d). This range is comparable to that estimated for tsunami earthquakes (e.g., 2006 Java M_w 7.8 tsunami earthquake which occurred close the Sunda trench and had a rupture velocity range of 1.0 – 1.5 km/s (Ammon et al., 2006)). Hence, the shallow earthquake (blue line in Fig. 4b), with its longer duration, small average stress drop and slow average rupture velocity, appears to be similar to the 1896 Meiji tsunami earthquake (Tanioka and Satake, 1996) (Fig. 1).

3.4 "Intermediate" depth earthquake

For the intermediate earthquake (orange line and dots, Figs 4-6), nucleation was in a zone where G^* and G_b^i are large (end of the rock to clay transition), but as rupture propagated up-dip the fault became weaker and G_b^i became smaller in the clay-rich material. Additionally, in thrust environments, seismic waves generated at depth by rupture and reflected back onto the fault by the free surface have been shown to induce tensile normal stress perturbations producing larger stress drops and slip near the surface (Nielsen, 1998; Oglesby et al., 1998) as well as promoting rupture in shallow velocity-strengthening environments (Kozdon and Dunham, 2013). This has also been noted in laboratory experiments where velocity strengthening clays at slow slip-rates and low effective normal stresses (< 30 MPa) become velocity weakening (Saffer and Marone, 2003) and have at the same time low G_b^i at slip-rates comparable to those observed during earthquakes (Faulkner et al., 2011). This means that rupture can easily propagate into clay-rich zones even when there is little initial shear stress present in the accretionary wedge.

This easier rupture propagation in clay-rich zones could explain the large size of 2011 Tohoku earthquake which nucleated at 20 – 25 km depth (Chu et al., 2011). In the case study, rupture travelled up-dip into the wedge, with a significant amount of slip occurring above 15 km depth, which is comparable to the slip inversions for the Tohoku earthquake (e.g. Romano et al., 2014, Fig. 1). The seismic moment release rate from the intermediate asperity is much larger and longer than the deepest and shallowest earthquakes (Fig. 6a) and produced the largest tsunami source (Fig. 6b). In some simulations where the asperity is located at a slightly deeper depth than the intermediate case study, rupture that initially propagates up-dip to the surface then propagated back down the fault again (Fig. 8c), this is a feature that has been suggested for the 2011 M_w 9 earthquake (Ide et al., 2011). Hence, we classify the intermediate simulation as a great thrust earthquake similar to the 2011 M_w 9.0 Tohoku earthquake.

3.5 "Deep" earthquakes

For the deep earthquakes, the distance between the asperity and the clay-rich trench is relevant. This is shown in Fig. 7e, where the earthquakes with the largest seismic moment release had centroid depths between 15 – 20 km. Below a certain depth of ~26 km, the distance from asperity to the clay-rich material was too far relative to the G^* for rupture to reach it; this produced a relatively smaller thrust earthquake (e.g., the ‘deep’ case study, purple line and dots, in Figs 4-6). These smaller thrust earthquakes had centroid depths below 20 km, had a larger stress drop (Fig. 7b), a faster rupture velocity (Fig. 7d) and larger average G_b^i (Fig. 7f) compared to the great thrust and tsunami earthquakes. They produced only one patch of significant slip making them comparable to the historical M_w 7 – 8 thrust earthquakes in Fig. 1.

4. Discussion

4.1 Varying scaling between principal stresses

Several assumptions were made in the construction of the numerical model. Therefore, a sensitivity study was performed to determine the robustness of the variation with depth of seismic ruptures features, in response to the initial parameters chosen in the model. For example, in the original set of simulations, the principal components of stress were assumed to have a $\sigma_1 = 4.05\,\sigma_3$. In an additional set of 15 simulations, this was changed to $\sigma_1 = 5.0\,\sigma_3$ to evaluate the effect of different regional principal stresses ratios. The value $\sigma_1 = 5.0\,\sigma_3$ was selected based on previous studies which used ratios of 4.7545 (Ma, 2012) and 5.0 (Brace and Kohlstedt, 1980). Comparing the average moment release, stress drop, G_b^i and rupture velocity per simulation (Fig. S8 in *Supplementary Material*), the change in principal stress ratios has not affected the depth dependent features observed in the original set of simulations.

4.2 Varying the fluid retention depth

Another test was done to examine the effect of altering the fluid retention depth, Z_{FRD}. Two additional sets of simulations (15 in each case) were run where z_{FRD} was shifted ± 5 km from the original depth, i.e. 7 km and 17 km. The effect on yield stress and initial stress distributions, can be viewed in the *Supplementary Material* (i.e. Fig. S4 for the original setup, Fig. S6 for Z_{FRD} = 7 km, and Fig. S7 for Z_{FRD} = 17 km in Section A5). Fig. 9 shows that the earthquakes in the ensemble with Z_{FRD} = 17 km produce more energetic earthquakes (i.e. large moment release and stress drop for intermediate size events). However, the general depth dependent trend observed in the original set of simulations (i.e., Z_{FRD} = 12 km) is still present. This is not the case when Z_{FRD} = 7 km where the depth dependent trends observed in the original study break down with earthquakes at depth exhibiting low rupture velocities (≈ 1 km/s) and long normalised duration. This breakdown in trend is due to the deeper sections of the fault becoming too weak (the yield stress drops below 20 MPa) to store sufficient elastic strain energy relative to the breakdown energy. For Z_{FRD} = 7 km there is still an increase in earthquake moment release at the transition from rock to clay-like material (between 10 - 20 km depth, Fig. 9a) albeit over a reduced scale both in terms of variation in moment and the spatial extent. Therefore, the effect of the rock-clay transition is still present, but as the strength of the deeper section of the fault has become comparable to the near-surface conditions this leads to a breakdown in the original depth-dependent trend.

4.3 Initial stress distributions

While the initial stress distributions used in these simulations were based on a single broad asperity model, in nature, the actual distribution is possibly more complex, and generally unknown. By lowering the initial stress below the residual shear stress outside of the asperity (i.e., $\tau < \mu_d \sigma_n$) rupture propagation was curtailed. Repeating the case studies presented in Fig. 4 with a higher initial stress outside of the asperity (i.e., $\tau = \mu_d \sigma_n$) produced similar slip distributions for the shallowest and deepest earthquakes (see Fig. 10). The intermediate depth earthquake was larger (with >50 m slip) in comparison with the original simulation. This is due to the intermediate earthquake nucleating near the strongest section of the fault which acts as a barrier in the other two cases. To continue to increase the initial shear stress outside of the asperity would ultimately lead to all earthquakes rupturing the full seismogenic zone with very little constraint on nucleation location and/or initial asperity location. Whether sections of the fault contain shear stress lower than the residual shear strength is unknown; phenomena such as dynamic overshoot and low coupling may contribute to it occurring. Alternative phenomena that would cause rupture arrest include increasing fault strength or G_b^i due to change in effective normal stress (i.e., due to changes in pore pressure/fault geometry) and/or frictional parameters (i.e., variations in fault material types). Our simplification provided a method for decoupling rupture features at different depths, and despite its limitations revealed itself effective in clarifying significant general relations between frictional properties and rupture dynamics in a subduction environment.

A less simplistic initial stress distributions could be achieved, for example, by considering multiple asperities of varying sizes on the fault plane. In such a situation rupture becomes more complex, for example rupture velocity and slip-rate have been shown to be strongly affected by sharp changes in initial shear stress and frictional parameters on the fault plane (Huang et al., 2013). In the simulations presented in this study, rupture velocity generally varies smoothly (see Fig. 8) with the exception being in certain cases when the asperity is located at intermediate depths where the rupture jumps to the very high pore pressure zone (Fig. 8c) due to this section of the fault being very weak. This effect could be negated by considering a highly compliant wedge or off-fault an-elastic deformation (as the current numerical model is purely elastic), particularly around the high pore pressure zone, which would slow down the rupture velocity (Lotto et al., 2017; Ma, 2012).

Finally, our pre-stress models are not derived from a complete description of a seismic cycle on the analysed fault, since our goal was to understand how depth-dependent frictional behavior may control, to first order, rupture dynamics.

4.4 Along strike variation of frictional parameters

The numerical models presented here are two dimensional and do not account for along strike heterogeneity (i.e. the fault is a line rather than a 2D surface). For example, strong variations in the fluid retention depth along the strike of the fault would lead to along strike variation in fault strength at depth. In our simulations, moving the fluid retention depth up 7 km weakened the fault at depth with the result that great earthquakes were no longer generated at depth (compare blue and black dots in Fig. 9). As demonstrated by the smaller size of earthquakes that nucleated at shallow depths in our ensemble of simulations, it is difficult for rupture to propagate into stronger patches of the fault. Shao et al. (2011) proposed that the repeat M7 earthquakes (i.e., 1981 and 2011) occur in relatively weak sections of the fault compared to a potential stronger patch where the 2011 M9 earthquake nucleated. This hypothesis is complementary to our findings whereby along strike variations in the fluid retention depth provides one possible mechanism to explain variations in strength. Other mechanisms such local changes in fault material, fault geometry and pore pressure are other potential means of causing along strike variations in fault strength. On a two-dimensional surface this additional complexity in turn makes rupture propagation more complex as it can conceivably go around barriers while the relative location of surrounding high stress asperities to nucleation can produce rupture directivity (Murphy and Nielsen, 2009). Consequently, while our 2D dynamic model produces depth dependent features similar to seismological observations (Bilek and Lay, 1999), further work involving 3D dynamic rupture simulations would be required to investigate the role of along strike heterogeneity. Particularly in explaining the difference between M7 earthquakes relative to the M9 2011 earthquake given that they nucleate at similar depths.

4.5 Friction Law

With the choice of slip weakening friction law, earthquake rupture was generally crack-like in the simulations (Fig. 8). Friction laws where fault strength evolves with slip rate are more likely to produce pulse-like ruptures (Nielsen and Carlson, 2000; Zheng and Rice, 1998), with shorter rise-time compared to crack-like ruptures. Additionally, velocity-strengthening zones near the surface can further complicate rupture dynamics (Kozdon and Dunham, 2013; Lotto et al., 2017). Consequently, it would be beneficial to perform studies with rate-based friction laws in the future.

Ultimately, the aim is to simulate the full seismic cycle with friction laws derived from experiments (and physical fault processes) that are consistent with conditions on the fault during the different stages of the seismic cycle. Nevertheless, despite the simplified framework provided by the single asperity model used here, our model manages to reproduce observed geophysical features between the different subduction zone earthquake types in this mega-thrust environment. The observed differences, can, to first order, be ascribed to rupture dynamics effects coupled with a depth-dependent friction law based that accounts for the expected geology at the Japan Trench.

4.6 Site specific nature of study

Our findings are regional as they are specific to the Tohoku trench environment. A meaningful extrapolation of these results to other subduction zones would require at least similarity in depth dependent frictional properties and fault geometry. For example, in this study, frictional properties based on a clay-like material was chosen as this was observed at Tohoku (Chester et al., 2013). However, soft sediment in the nearby Nankai trench is more sandy in nature (Hirono et al., 2014). Dynamic simulations comparing the two environments have shown that a more sandy sediment produces a larger thermal pressurisation during dynamic rupture but this is offset by higher initial excess fluid pressure (Hirono et al., 2016). Consequently, care must be taken in applying the finds from one subduction zone to another.

5. Conclusion

In nature, subduction zone faults are more complicated than what is depicted in our numerical models (fault roughness, multiple asperities, off-fault an-elastic deformation etc.). In particular, our choice of type of initial stress distribution (i.e. an 'asperity' model) only examines a small part of the potential stress models and it might not be compatible with stress profiles derived from the modelling of the whole seismic cycle. Therefore, future work should focus on the application of the model to a much wider range of heterogeneous initial stress conditions.

Nevertheless, our model based on lithological and depth dependent friction law tuned to the 2011 Tohoku fault region allows us to better understand and reproduce to the first order the different types of (tsunamigenic) earthquakes. Consistently with geophysical observations, the numerical simulations have shown that events with a number of characteristics resembling tsunami earthquakes were generated either near to or below the accretionary wedge. Their rupture area was constrained to remain there due to the fault strength and breakdown energy increasing with depth. We also found that standard thrust earthquakes, with relatively larger stress drops, shorter durations and faster rupture velocities occurred in crystalline rock where both the energy release rate and fault resistance are high. Finally, if the rupture initiated at the bottom of or just below the rock-clay transition and propagated towards the surface and into a zone characterised by low fault strength and frictional resistance, this leads to the production of great thrust earthquakes.

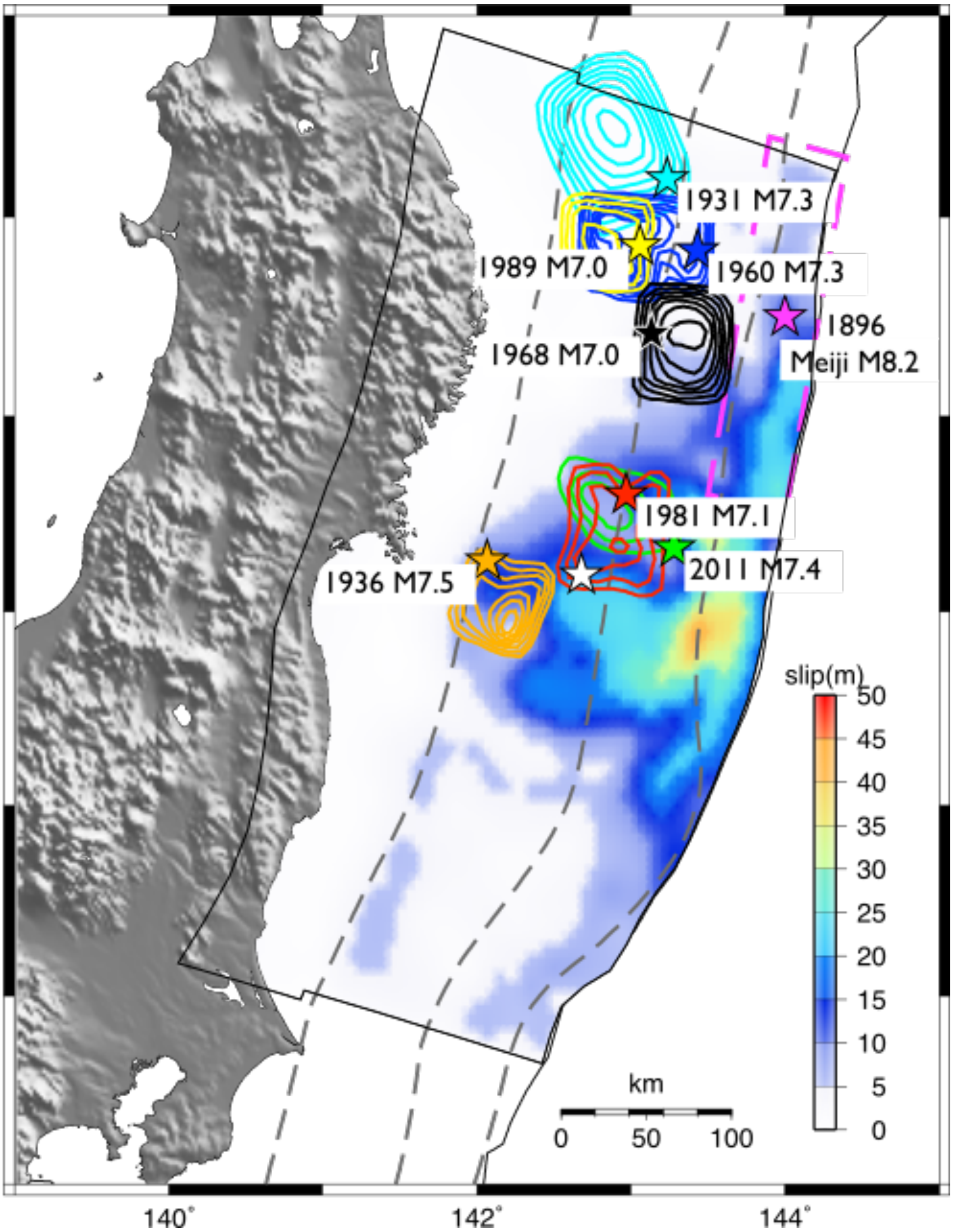

Figure 1: Earthquake history off the Pacific coast of Tohoku region and model setup. Coloured contours represent slip distributions at 0.5 m interval for a number of

historical thrust earthquakes(Shao et al., 2011; Yamanaka and Kikuchi, 2004); The magenta dashed box represents the location for the 1896 Meiji tsunami earthquakes (M 8.2-8.4). The colour slip distribution is the M_w 9 Tohoku earthquake(Romano et al., 2014), the red star is its epicentre. Dashed grey line is depth at 10, 20 and 40 km.

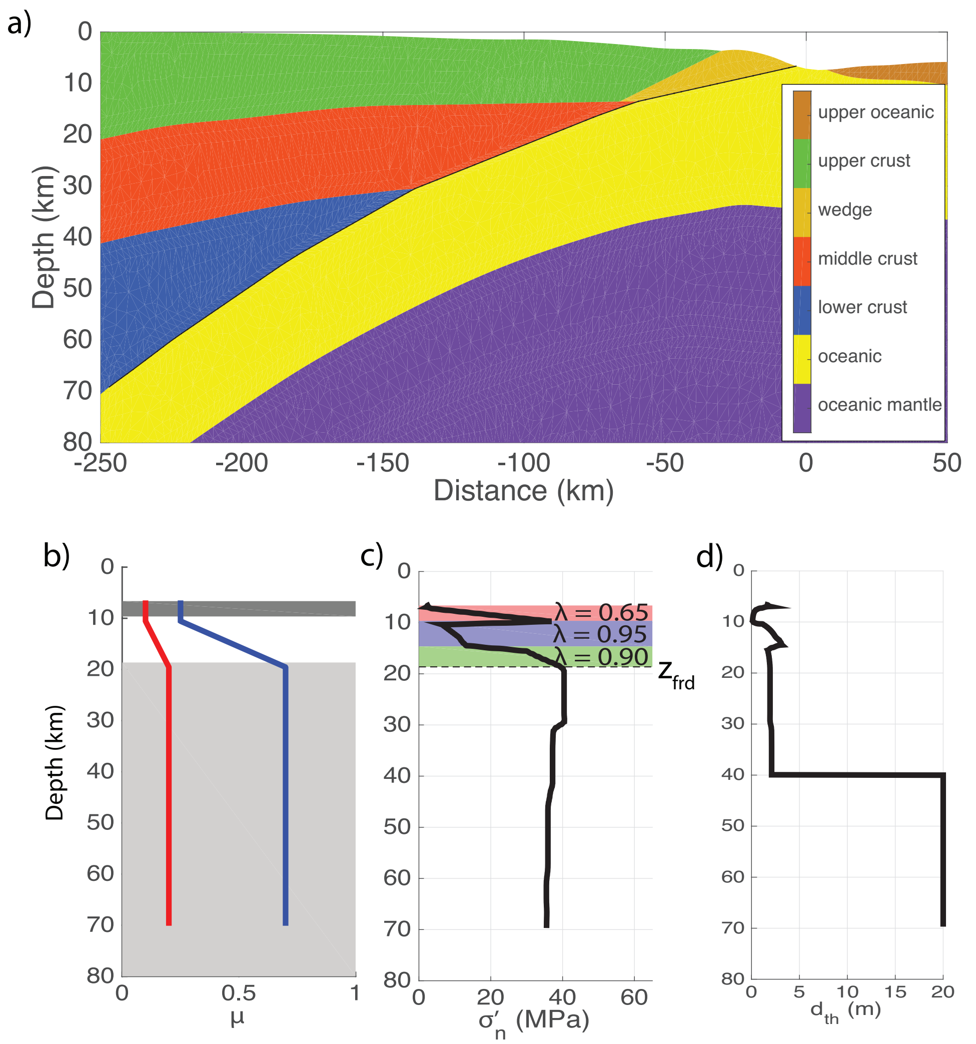

Figure 2: Numerical model set up. **a)** structural model used in the numerical simulations, black line denotes the subduction interface. **b)** variation of frictional coefficients with depth: the dark and light grey boxes denote the clay-rich and crystalline rock frictional coefficients; the white is the transition between the two

materials. Solid blue and red lines are the static and dynamic coseismic coefficients of friction respectively. **c)** the variation of the effective normal stress with depth, coloured boxes denote different pore fluid to overburden stress ratio, λ. The dashed black line denotes the fluid retention depth. **d)** variance of d_{th} with depth which is a function of effective normal stress and frictional material type (i.e., rock or clay-rich).

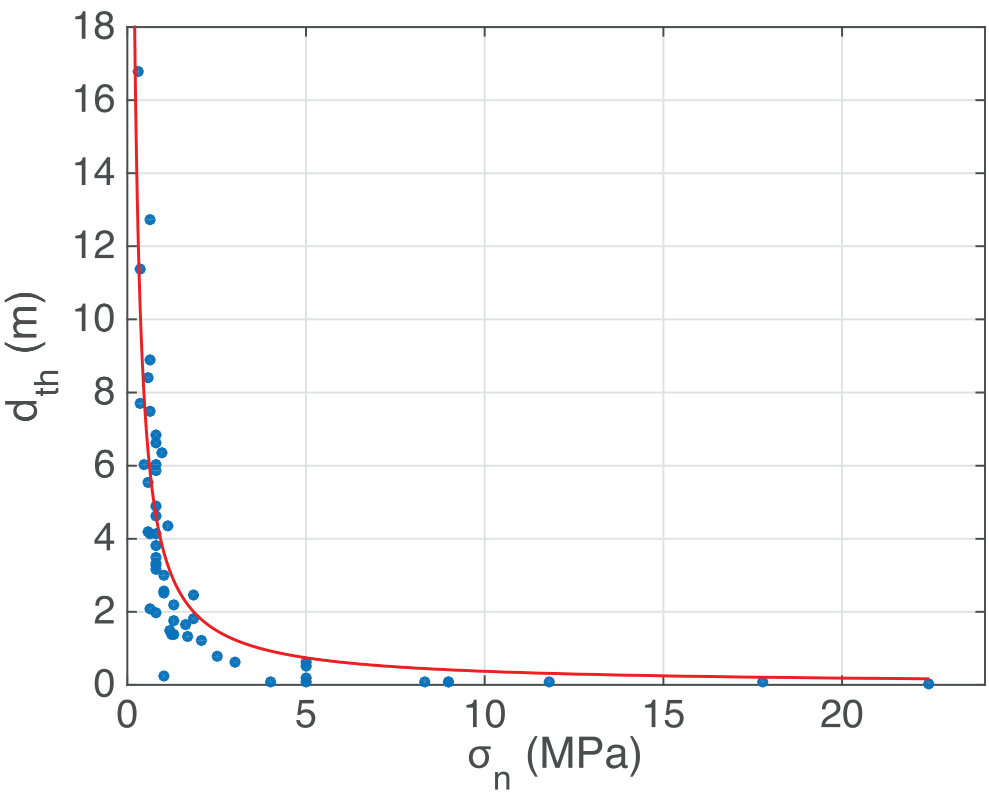

Figure 3: The fit of $d_{th} = 3.712\ \|\sigma_n\|^{-1}$ (red line) compared with the laboratory experiments performed on clay material (see Table S5 in *Supplementary Material* for references).

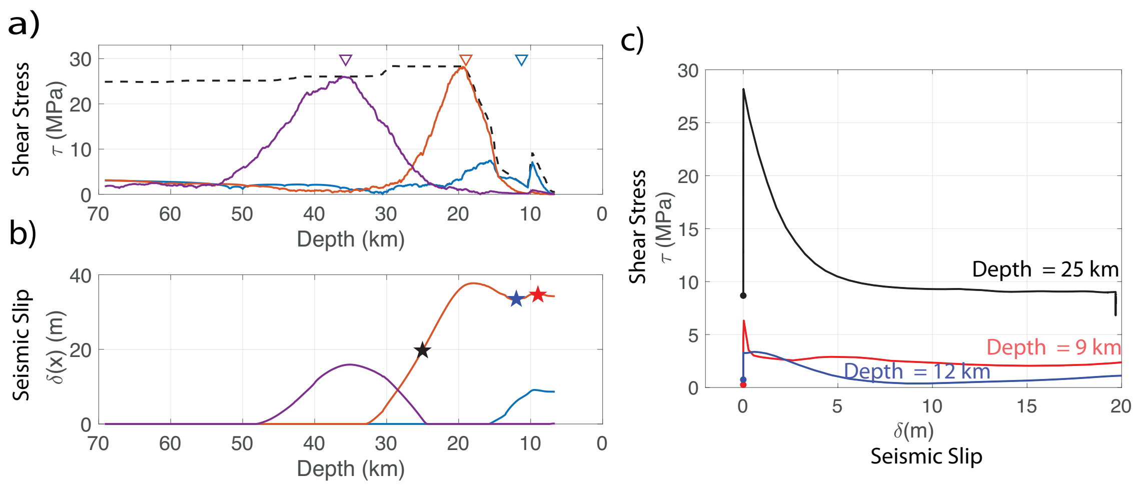

Figure 4: Modelled environment earthquake source parameters **a)** The different solid colours relate to the initial shear stress distributions used in the three simulations which reproduce a tsunamigenic great thrust earthquake (orange), tsunami earthquake (blue) and thrust earthquakes (purple). The same colour code is used for all subplots. Triangles are nucleation locations. Black dashed line is the fault strength. **b)** Slip distributions resulting from simulations where the colours relate to the initial stress distributions in a). **c)** Shear stress evolution with slip at three different depths (25 km black line, 12 km blue line, 9 km red line) taken from intermediate simulation (i.e., orange line in b). The locations are also highlighted by stars in subplot b) where a similar colour scale has been used. Dots denote the initial stress at each location.

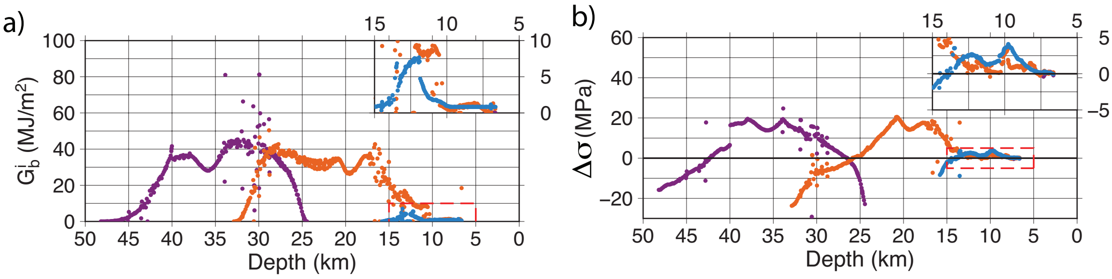

Figure 5: **a)** Breakdown energy calculated at each point along the fault. Insets are expansions of the data inside the red dashed boxes. **b)** Static stress drop calculated at each point along the fault.

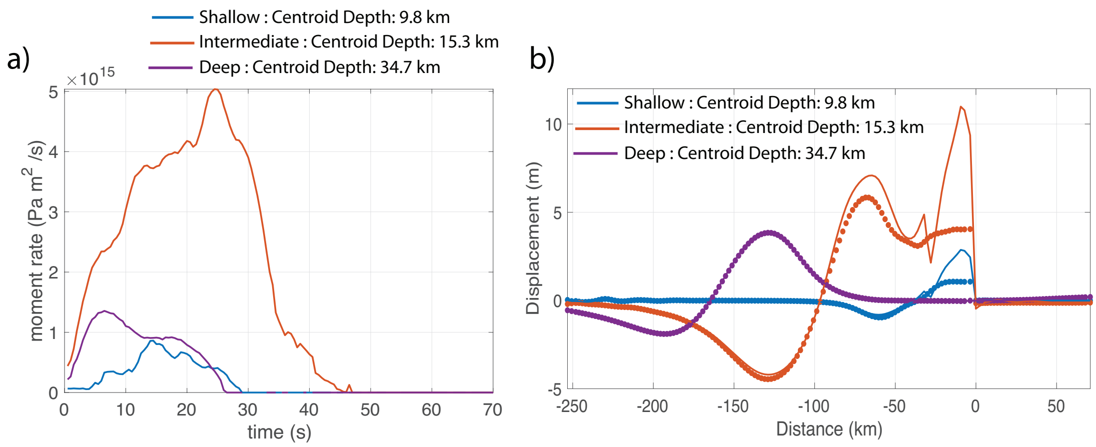

Figure 6: **a)** Moment release rate with time. **b)** Vertical seafloor displacement (dotted lines) and estimated tsunami source (solid lines, details in Section A3 in *Supplementary Information*). Horizontal distance as in Fig. 2 where 0 km indicates the point where the fault reaches the seafloor.

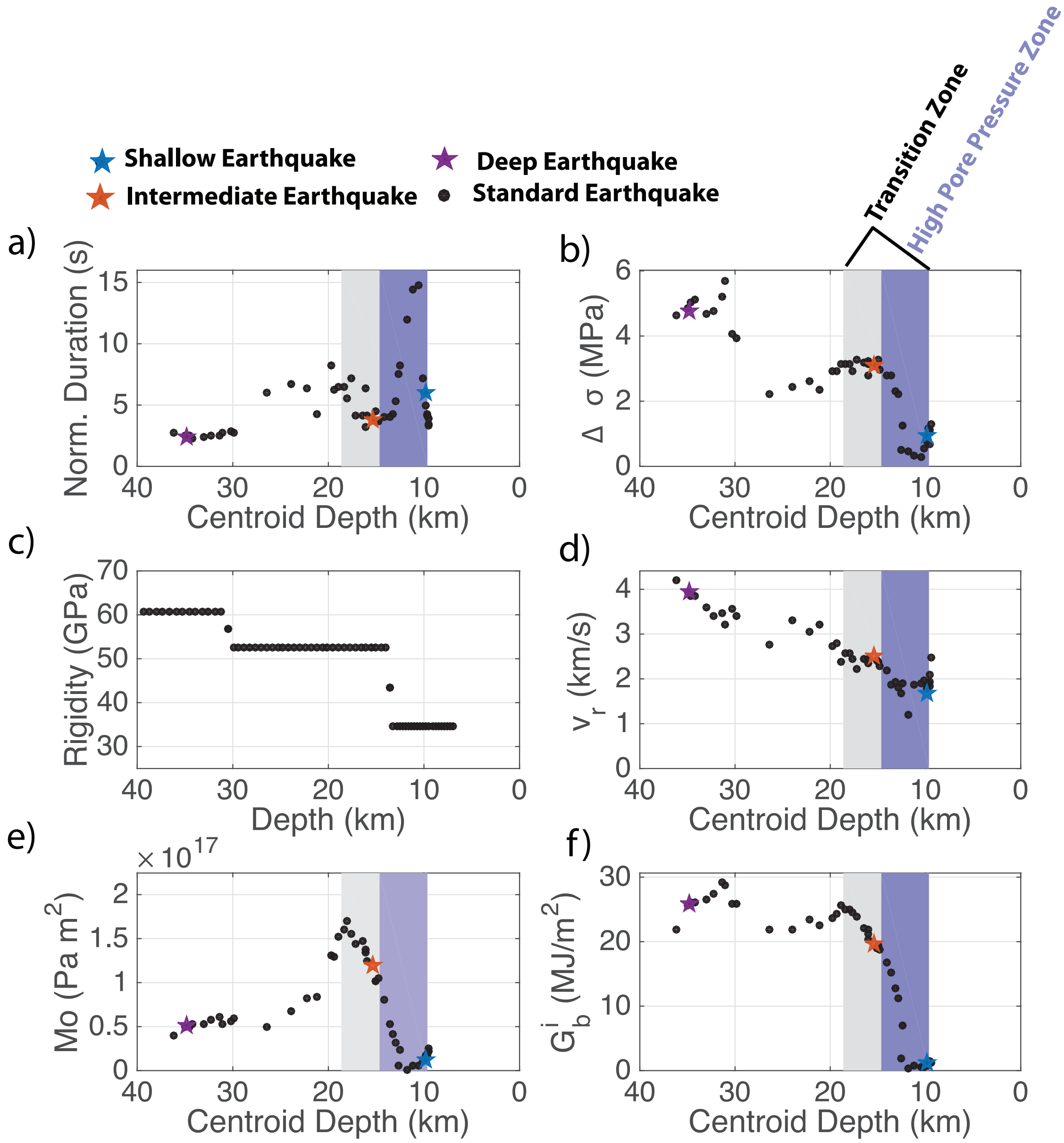

Figure 7: Rupture parameters plotted against centroid depth for a number of simulations where only the location of the high stress asperity varies with depth. The purple box is the zone with very high pore pressure ($\lambda = 0.95$); grey and purple boxes together demark the transition zone between clay-like and crystalline rock frictional parameters. **a)** Normalised earthquake duration; **b)** Average static stress drop; **c)** shear modulus averaged across the fault plane to account of bi-material wall rocks; **d)** Average rupture velocity; **e)** Moment of the (1D) simulated earthquakes (details in

Section A4 in *Supplementary Material*); and **f)** Average breakdown energy. The stars indicate the three case studies presented in Fig. 2 with the same colour code applied.

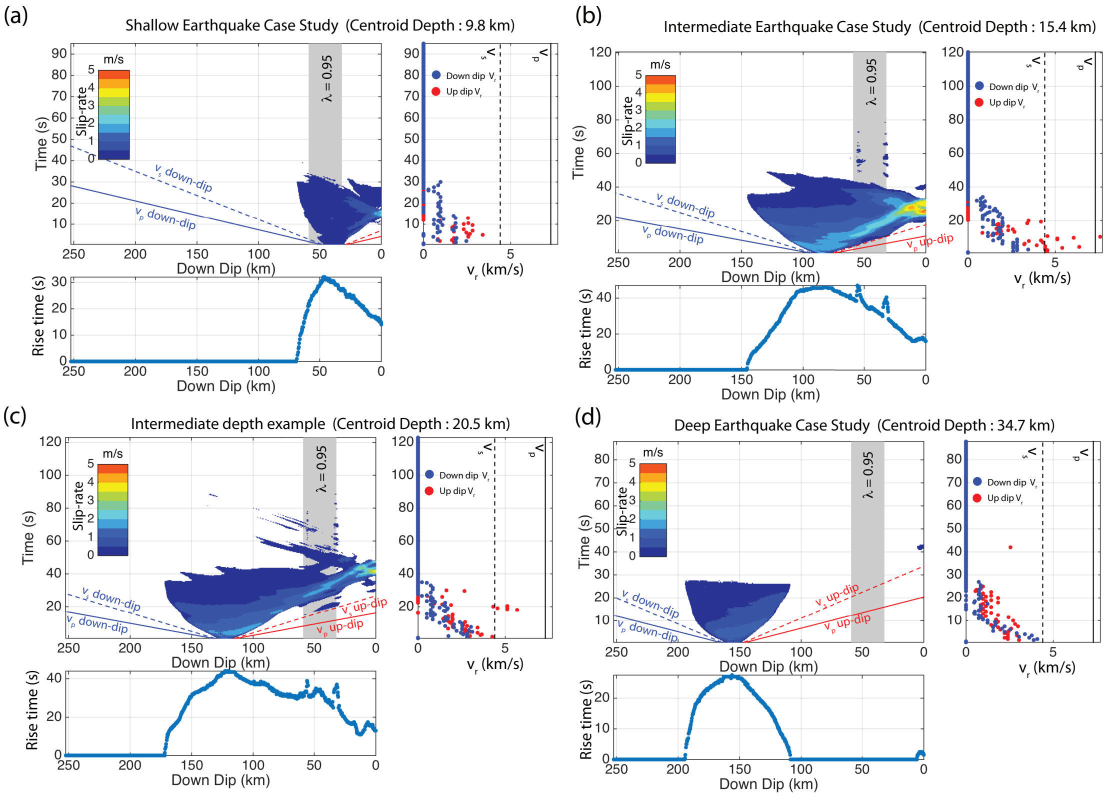

Figure 8: Slip-rate, rupture velocity and rise-time observed in four simulations with increasing fault down-dip location of the asperity (40, 80, 120 and 160 km depth, respectively). These depths correspond to the hypocentral depths of the three cases presented in Fig. 2 and an additional great thrust earthquake which generated a down-dip travelling rupture pulse. In all subplots the solid and dashed lines are the P- and S-wave velocities in the oceanic material (i.e., yellow layer in Fig. 1) with the colour of the line indicating rupture direction (i.e. blue is to the left of the nucleation zone or down-dip, red is the right or up-dip). The light grey box behind the slip-rates defines the zone of very high pore pressure (i.e., λ = 0.95) in the wedge. **a)** Asperity in the

wedge which corresponds to the shallow case study (blue line and dots in Figs. 2 and 3) **b)** Asperity at 20 km depth related to the intermediate case study (i.e., orange data in Figs. 2 and 3). **c)** Asperity at 27 km depth, an example of a great thrust earthquake with a down-dip travelling rupture pulse that was referred to in Section 3.4 **d)** Deep case study (i.e., 39 km) purple colour in Figs. 2 and 3.

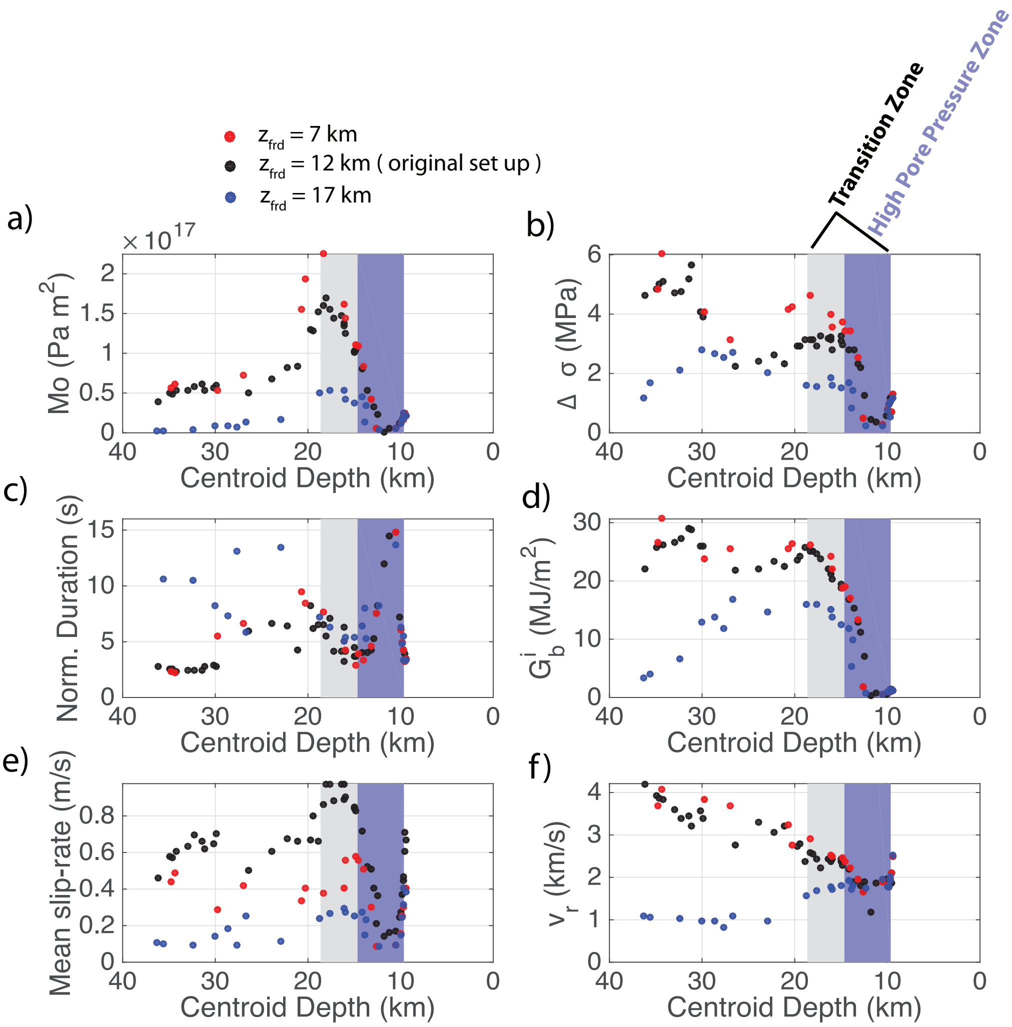

Figure 9: Sensitivity study on varying the fluid retention depth. The black dots are from simulations using the original model discussed in Section 3 (i.e., z_{FRD} = 12 km)

with 45 simulations, the blue dots are the case z_{FRD} = 7 km (15 simulations) and the red dots are case with z_{FRD} = 17 km (15 simulations). **a)** Seismic moment of the simulated earthquake; a constant shear modulus G = 30 GPa rather than a depth dependent shear modulus was used in the calculation as it is commonly used in observational seismology, **b)** Average static stress drop, **c)** average normalised rupture duration, **d)** average breakdown energy, **e)** average slip-rate per earthquake and **f)** average rupture velocity.

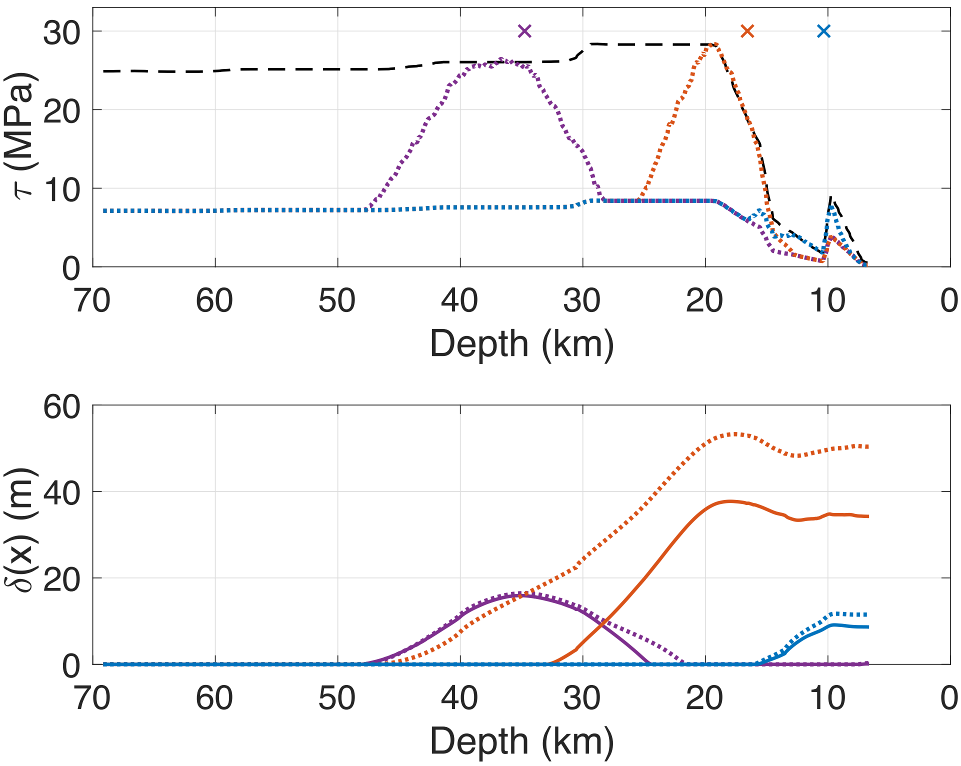

Figure 10: Testing increased background initial stress outside of the asperity. **a)** The black dashed line is the yield strength. The dotted colour lines represent the initial shear stress where stress does not drop below the residual shear stress (i.e. $\tau = \mu_d \sigma_n$). The x's are the nucleation locations for the new (i.e. dashed) set of simulations. **b)** the final slip distributions for each simulation where the colour and line type convention

is same as the one used in subplot a) The solid lines are the slip distributions using the original initial stress distribution (see Fig. 4).

References

Abercrombie, R., Rice, J., 2005. Can observations of earthquakes scaling constrain slip weakening. Geophys. J. Int. 162, 406–424. doi:10.1111/j.1365-246X.2005.02579.x

Ammon, C.J., Kanamori, H., Lay, T., Velasco, A.A., 2006. The 17 July 2006 Java tsunami earthquake. Geophys. Res. Lett 33, L24308–5. doi:10.1029/2006GL028005

Bilek, S.L., Lay, T., 1999. Rigidity variations with depth along interplate megathrust faults in subduction zones. Nature 400, 443–446. doi:10.1038/22739

Bilek, S.L., Rotman, H.M.M., Phillips, W.S., 2016. Low stress drop earthquakes in the rupture zone of the 1992 Nicaragua tsunami earthquake. Geophys. Res. Lett 43, 10,180–10,188. doi:10.1002/2016GL070409

Brace, W.F., Kohlstedt, D.L., 1980. Limits on lithospheric stress imposed by laboratory experiments. J. Geophys. Res. 85, 6248–6252. doi:10.1029/JB085iB11p06248

Chester, F.M., Rowe, C., Ujiie, K., Kirkpatrick, J., Regalla, C., Remitti, F., Moore, J.C., Toy, V., Wolfson-Schwehr, M., Bose, S., Kameda, J., Mori, J.J., Brodsky, E.E., Eguchi, N., Toczko, S., Expedition 343 and 343T Scientists, 2013. Structure and Composition of the Plate-Boundary Slip Zone for the 2011 Tohoku-Oki Earthquake. Science 342, 1208–1211. doi:10.1126/science.1243719

Chu, R., Wei, S., Helmberger, D.V., Zhan, Z., Zhu, L., Kanamori, H., 2011. Initiation of the great Mw 9.0 Tohoku–Oki earthquake. Earth Planet. Sci. Lett. 308, 277–283. doi:10.1016/j.epsl.2011.06.031

Cochard, A., Madariaga, R., 1996. Complexity of seismicity due to highly rate-dependent friction. J. Geophys. Res. 101, 25,321–25,336.

Cubas, N., Lapusta, N., Avouac, J.-P., Perfettini, H., 2015. Numerical modeling of long-term earthquake sequences on the NE Japan megathrust: Comparison with observations and implications for fault friction. Earth Planet. Sci. Lett. 419, 187–198. doi:10.1016/j.epsl.2015.03.002

Del Gaudio, P., Di Toro, G., Han, R., Hirose, T., Nielsen, S., Shimamoto, T., Cavallo, A., 2009. Frictional melting of peridotite and seismic slip. J. Geophys. Res. 114, B06306–19. doi:10.1029/2008JB005990

Di Toro, G., Han, R., Hirose, T., De Paola, N., Nielsen, S., Mizoguchi, K., Ferri, F., Cocco, M., Shimamoto, T., 2011. Fault lubrication during earthquakes. Nature 471, 494–498. doi:10.1038/nature09838

Dieterich, J., 1979. Modeling of Rock Friciton: 1. Experimental results and constituive equations. J. Geophys. Res. 84, 2161–2168.

Faulkner, D.R., Mitchell, T.M., Behnsen, J., Hirose, T., Shimamoto, T., 2011. Stuck in the mud? Earthquake nucleation and propagation through accretionary forearcs. Geophys. Res. Lett 38. doi:10.1029/2011GL048552

Festa, G., Vilotte, J.-P., 2005. The Newmark scheme as velocity–stress timestaggering: an efficient PML implementation for spectral element simulations of elastodynamics. Geophys. J. Int. 161, 789–812. doi:10.1111/j.1365-246X.2005.02601.x

Festa, G., and J.-P. Vilotte 2006, Influence of the rupture initiation on the intersonic transition: Crack-like versus pulse-like modes, Geophys. Res. Lett,, 33 (L15320), doi:http://dx.doi.org/10.1029/2006GL026378.

Freed, A., 2005. Earthquake triggering by static, dynamic, and postseismic stress transfer. Annu. Rev. Earth Planet Sci. 33, 335–367. doi:http://dx.doi.org/10.1146/annurev.earth.33.092203.122505

Gao, X., Wang, K., 2014. Strength of stick-slip and creeping subduction megathrusts from heat flow observations. Science 345, 1038–1041. doi:10.1126/science.1255487

Geist, E.L., Bilek, S.L., 2001. Effect of depth-dependent shear modulus on tsunami generation along subduction zones. Geophys. Res. Lett 28, 1315–1318. doi:10.1029/2000GL012385

Grezio, A., Babeyko, A., Baptista, M. A., Behrens, J., Costa, A., Davies, G., Geist, E. L., Glimsdal, S., González, F. I., Griffin, J., Harbitz, C. B., LeVeque, R. J., Lorito, S., Løvholt, F., Omira, R., Mueller, C., Paris, R., Parsons, T., Polet, J., Power, W., Selva, J., Sørensen M., B., Thio, H. K. 2017. Probabilistic Tsunami Hazard Analysis: Multiple sources and global applications. Reviews of Geophysics, 55. doi: 10.1002/2017RG000579

Hacker, B.R., Abers, G.A., Peacock, S.M., 2003a. Subduction factory 1. Theoretical mineralogy, densities, seismic wave speeds, and H2O contents. J Geophys Res 108, 1–26. doi:10.1029/2001JB001127

Hacker, B.R., Peacock, S.M., Abers, G.A., Holloway, S.D., 2003b. Subduction factory 2. Are intermediate-depth earthquakes in subducting slabs linked to metamorphic dehydration reactions? J. Geophys. Res. 108, 1–20. doi:10.1029/2001JB001129

Hartog, den, S.A.M., Niemeijer, A.R., Spiers, C.J., 2012. New constraints on megathrust slip stability under subduction zone P–T conditions. Earth and Planetary Science Letters 353-354, 240–252. doi:10.1016/j.epsl.2012.08.022

Hayes, G.P., Wald, D.J., Johnson, R.L., 2012. Slab1.0: A three-dimensional model of global subduction zone geometries. J. Geophys. Res. 117, B01302–15. doi:10.1029/2011JB008524

Hirono, T., Ishikawa, T., Masumoto, H., Kameda, J., Yabuta, H., Mukoyoshi, H., 2014. Re-evaluation of frictional heat recorded in the dark gouge of the shallow part of a megasplay fault at the Nankai Trough. Tectonophysics 626, 157–169. doi:10.1016/j.tecto.2014.04.020

Hirono, T., Tsuda, K., Tanikawa, W., Ampuero, J.-P., Shibazaki, B., Kinoshita, M., Mori, J.J., 2016. Near-trench slip potential of megaquakes evaluated from fault properties and conditions. Sci. Rep. 1–13. doi:10.1038/srep28184

Huang, Y., Ampuero, J.-P., Kanamori, H., 2013. Slip-Weakening Models of the 2011 Tohoku-Oki Earthquake and Constraints on Stress Drop and Fracture Energy. Pure Appl. Geophys. 171, 2555–2568. doi:10.1007/s00024-013-0718-2

Hyndman, R., Yamano, M., Oleskevich, D., 1997. The seismogenic zone of subduction thrust faults. The Island Arc 6, 244–260.

Ida, Y., 1972. Cohesive Force across the Tip of a Longitudinal-Shear Crack and Griffith's Specific Surface Energy. J. Geophys. Res. 77, 3796–3805.

Ide, S., Baltay, A., Beroza, G.C., 2011. Shallow Dynamic Overshoot and Energetic Deep Rupture in the 2011 Mw 9.0 Tohoku-Oki Earthquake. Science 332, 1426–

1429. doi:10.1126/science.1207020

Ihmlé, P.F., 1996. Monte Carlo slip inversion in the frequency domain:: Application to the 1992 Nicaragua Slow Earthquake. Geophys. Res. Lett 23, 913–916. doi:10.1029/96GL00872

Ikari, M.J., Saffer, D.M., Marone, C., 2007. Effect of hydration state on the frictional properties of montmorillonite-based fault gouge. J. Geophys. Res. 112, B06423–12. doi:10.1029/2006JB004748

Kanamori, H., 1972. Mechanism of tsunami earthquakes. Phys. Earth Planet. In. 6, 346–359. doi:10.1016/0031-9201(72)90058-1

Kato, N., 2012. Dependence of earthquake stress drop on critical slip-weakening distance. J Geophys Res 117. doi:10.1029/2011JB008359

Kimura, G., Hina, S., Hamada, Y., Kameda, J., Tsuji, T., Kinoshita, M., Yamaguchi, A., 2012. Runaway slip to the trench due to rupture of highly pressurized megathrust beneath the middle trench slope: The tsunamigenesis of the 2011 Tohoku earthquake off the east coast of northern Japan. Earth Planet. Sci. Lett. 339-340, 32–45. doi:10.1016/j.epsl.2012.04.002

Kozdon, J.E., Dunham, E.M., 2014. Constraining shallow slip and tsunami excitation in megathrust ruptures using seismic and ocean acoustic waves recorded on ocean-bottom sensor networks. Earth Planet. Sci. Lett. 396, 56–65. doi:10.1016/j.epsl.2014.04.001

Kozdon, J.E., Dunham, E.M., 2013. Rupture to the Trench: Dynamic Rupture Simulations of the 11 March 2011 Tohoku Earthquake. B. Seismol. Soc. Am. 103, 1275–1289. doi:10.1785/0120120136

Lay, T., Kanamori, H., Ammon, C.J., Koper, K.D., Hutko, A.R., Ye, L., Yue, H., Rushing, T.M., 2012. Depth-varying rupture properties of subduction zone megathrust faults. J. Geophys. Res. 117, B04311–21. doi:10.1029/2011JB009133

Lorito, S., Romano, F., & Lay, T., 2016. Tsunamigenic earthquakes (2004–2013): Source processes from data inversion. In R. Meyers (Ed.)*, Encyclopedia of complexity and systems science.* New York: Springer Science+Business Media New York 2015. doi: 10.1007/978-3-642-27737-5641-1

Lotto, G.C., Dunham, E.M., Jeppson, T.N., Tobin, H.J., 2017. The effect of compliant prisms on subduction zone earthquakes and tsunamis. Earth Planet. Sci. Lett. 458, 213–222. doi:10.1016/j.epsl.2016.10.050

Ma, S., 2012. A self-consistent mechanism for slow dynamic deformation and tsunami generation for earthquakes in the shallow subduction zone. Geophys. Res. Lett 39, n/a–n/a. doi:10.1029/2012GL051854

Meneghini, F., Di Toro, G., Rowe, C.D., Moore, J.C., Tsutsumi, A., Yamaguchi, A., 2010. Record of mega-earthquakes in subduction thrusts: The black fault rocks of Pasagshak Point (Kodiak Island, Alaska). Geol. Soc. Am. Bull. 122, 1280–1297. doi:10.1130/B30049.1

Mitsui, Y., Yagi, Y., 2013. An interpretation of tsunami earthquake based on a simple dynamic model: Failure of shallow megathrust earthquake. Geophys. Res. Lett 40, 1523–1527. doi:10.1002/grl.50266

Miura, S., Takahashi, N., Nakanishi, A., Tsuru, T., Kodaira, S., Kaneda, Y., 2005. Structural characteristics off Miyagi forearc region, the Japan Trench seismogenic zone, deduced from a wide-angle reflection and refraction study. Tectonophysics 407, 165–188. doi:10.1016/j.tecto.2005.08.001

Murphy, S., Nielsen, S., 2009. Estimating earthquake magnitude with early arrivals: A test using dynamic and kinematic models. B. Seismol. Soc. Am. 99, No. 1, 1–23. doi:http://dx.doi.org/10.1785/0120070246

Murphy, S., Scala, A., Herrero, A., Lorito, S., Festa, G., Trasatti, E., Tonini, R., Romano, F., Molinari, I., Nielsen, S., 2016. Shallow slip amplification and enhanced tsunami hazard unravelled by dynamic simulations of mega-thrust earthquakes. Sci. Rep. 1–12. doi:10.1038/srep35007

Nalbant, S., McCloskey, J., Steacy, S., NicBhloscaidh, M., Murphy, S., 2013. Interseismic coupling, stress evolution, and earthquake slip on the Sunda megathrust. Geophys. Res. Lett 40, 4204–4208. doi:10.1002/grl.50776

Nielsen, S., Carlson, J., 2000. Rupture Pulse Characterization: Self-Healing, Self-Similar, Expanding Solutions in a Continuum Model of Fault Dynamic. B. Seismol. Soc. Am. 90, No. 6, 1480–1497.

Nielsen, S., Mosca, P., Giberti, G., Di Toro, G., Hirose, T., Shimamoto, T., 2010. On the transient behavior of frictional melt during seismic slip. J. Geophys. Res. 115, B10301–17. doi:10.1029/2009JB007020

Nielsen, S., Spagnuolo, E., Violay, M., Smith, S., Toro, G., Bistacchi, A., 2016. G: Fracture energy, friction and dissipation in earthquakes. J. Seismol. 1–19. doi:10.1007/s10950-016-9560-1

Nielsen, S.B., 1998. Free surface effects on the propagation of dynamic rupture. Geophys. Res. Lett. 25, 125–128.

Niemeijer, A., Di Toro, G., Nielsen, S., Di Felice, F., 2011. Frictional melting of gabbro under extreme experimental conditions of normal stress, acceleration, and sliding velocity. J. Geophys. Res. 116. doi:10.1029/2010JB008181

Noda, H., Lapusta, N., 2013. Stable creeping fault segments can become destructive as a result of dynamic weakening. Nature 493, 518–521. doi:10.1038/nature11703

Oglesby, D., Archuleta, R., Nielsen, S., 1998. Earthquakes on Dipping Faults: The Effects of Broken Symmetry. Science 280, 1055–1059. doi:http://dx.doi.org/10.1126/science.280.5366.1055

Ozawa, S., Nishimura, T., Suito, H., Kobayashi, T., Tobita, M., Imakiire, T., 2011. Coseismic and postseismic slip of the 2011 magnitude-9 Tohoku-Oki earthquake. Nature 475, 373–376. doi:10.1038/nature10227

Proctor, B.P., Mitchell, T.M., Hirth, G., Goldsby, D., Zorzi, F., Platt, J.D., Di Toro, G., 2014. Dynamic weakening of serpentinite gouges and bare surfaces at seismic slip rates. J. Geophys. Res. 119, 8107–8131. doi:10.1002/2014JB011057

Remitti, F., Smith, S.A.F., Mittempergher, S., Gualtieri, A.F., Di Toro, G., 2015. Frictional properties of fault zone gouges from the J-FAST drilling project (M w9.0 2011 Tohoku-Oki earthquake). Geophys. Res. Lett 42, 2691–2699. doi:10.1002/2015GL063507

Romano, F., Trasatti, E., Lorito, S., Piromallo, C., Piatanesi, A., Ito, Y., Zhao, D., Hirata, K., Lanucara, P., Cocco, M., 2014. Structural control on the Tohoku earthquake rupture process investigated by 3D FEM, tsunami and geodetic data. Sci. Rep. 4. doi:10.1038/srep05631

Rubin, A.M., Ampuero, J.-P., 2007. Aftershock asymmetry on a bimaterial interface. Journal of Geophysical Research 112, B05307–23. doi:10.1029/2006JB004337

Ruina, A., 1983. Slip instablity and state variable friction law. J. Geophys. Res. 88, 10359–10370.

Saffer, D.M., Lockner, D.A., McKiernan, A., 2012. Effects of smectite to illite transformation on the frictional strength and sliding stability of intact marine mudstones. Geophys. Res. Lett. 39, L11304. doi:10.1029/2012GL051761

Saffer, D.M., Marone, C., 2003. Comparison of smectite- and illite-rich gouge frictional properties: application to the updip limit of the seismogenic zone along subduction megathrusts. Earth Planet. Sci. Lett. 215, 219–235.

doi:10.1016/S0012-821X(03)00424-2

Satake, K., Tanioka, Y., 1999. Sources of Tsunami and Tsunamigenic Earthquakes in Subduction Zones, in: Seismogenic and Tsunamigenic Processes in Shallow Subduction Zones. Pure Appl. Geophys. 154, 467–483. doi:10.1007/978-3-0348-8679-6_5

Sawai, M., Hirose, T., Kameda, J., 2014. Frictional properties of incoming pelagic sediments at the Japan Trench: implications for large slip at a shallow plate boundary during the 2011 Tohoku earthquake. Earth, Planets Space 66, 65. doi:10.1186/1880-5981-66-65

Scala, A., Festa, G., Vilotte, J.-P., 2017. Rupture dynamics along bimaterial interfaces: a parametric study of the shear-normal traction coupling. Geophys. J. Int. 209, 1. doi:10.1093/gji/ggw489

Shao, G., Ji, C., Zhao, D., 2011. Rupture process of the 9 March, 2011 Mw 7.4 Sanriku-Oki, Japan earthquake constrained by jointly inverting teleseismic waveforms, strong motion data and GPS observations. Geophys. Res. Lett. 38, L00G20. doi:10.1029/2011GL049164

Shibazaki, B., Matsuzawa, T., Tsutsumi, A., 2011. 3D modeling of the cycle of a great Tohoku-Oki earthquake, considering frictional behavior at low to high slip velocities. Gephys. Res. Lett. 38, L21305. doi: 10.1029/2011GL049308

Suppe, J., 2014. Fluid overpressures and strength of the sedimentary upper crust. J. Struct. Geol. 69, 481-492. doi:10.1016/j.jsg.2014.07.009

Tanioka, Y., Satake, K., 1996. Fault parameters of the 1896 Sanriku Tsunami Earthquake estimated from Tsunami Numerical Modeling. Geophys. Res. Lett 23, 1549–1552. doi:10.1029/96GL01479

Ujiie, K., Tanaka, H., Saito, T., Tsutsumi, A., Mori, J.J., Kameda, J., Brodsky, E.E., Chester, F.M., Eguchi, N., Toczko, S., Expedition 343 and 343T Scientists, 2013. Low Coseismic Shear Stress on the Tohoku-Oki Megathrust Determined from Laboratory Experiments. Science 342, 1211–1214. doi:10.1126/science.1243485

Violay, M., Di Toro, G., Gibert, B., Nielsen, S., Spagnuolo, E., Del Gaudio, P., Azais, P., Scarlato, P.G., 2014. Effect of glass on the frictional behavior of basalts at seismic slip rates. Geophys. Res. Lett. 41, 348–355. doi:10.1002/ 2013GL058601

Wang, K., Hu, Y., 2006. Accretionary prisms in subduction earthquake cycles: The theory of dynamic Coulomb wedge. J. Geophys. Res. 111, B06410. doi:10.1029/2005JB004094

Wang, K., Hu, Y., Huene, von, R., Kukowski, N., 2010. Interplate earthquakes as a driver of shallow subduction erosion. Geology 38, 431–434. doi:10.1130/G30597.1

Yamanaka, Y., Kikuchi, M., 2004. Asperity map along the subduction zone in northeastern Japan inferred from regional seismic data. J. Geophys. Res. 109, 1–16. doi:10.1029/2003JB002683

Zheng, G., and Rice J., 1998. Conditions under which Velocity-Weakening Friction Allows a Self-healing versus a Cracklike Mode of Rupture, *BSSA*, *88, No. 6*, 1466–1483.

Acknowledgements: S.M., G.D.T., E.S., S.N., S.A. were supported by the European Research Council Consolidator Grant Project No. 614705 NOFEAR . S.L. and A.P were supported by the European Union's Seventh Framework Programme (FP7/2007-

2013) under grant agreement n° 603839 (Project ASTARTE - Assessment, Strategy and Risk Reduction for Tsunamis in Europe). All of the figures have been created using either MATLAB (www.mathworks.com) and Generic Mapping Tools (http://gmt.soest.hawaii.edu). Two anonymous reviewers and the Editor are acknowledged for their constructive comments which further improved the paper.

Author Contributions: S.M. performed the numerical simulations. G.D.T., E.S., S.A. and S.N. provided frictional parameters for numerical models from both experiments they performed and literature. F.R. digitised slip distributions from historical earthquakes. Tsunami source estimates provided by F.R. and A.S.; G.F. and A.S. developed the numerical code. Concept development: S.M., G.D.T., S.L. and E.S; important ideas provided by S.N., G.F. and A.P. throughout the development of the work. All authors contributed to text and revised the manuscript several times.

Additional Information

The authors declare no competing financial interests. Correspondence and requests for materials should be addressed to S.M. (shane.murphy@ifremer.fr).